X-Tream quality assurance in synchrotron X-ray microbeam radiation therapy

Pauline Fournier,[a]* Iwan Cornelius,[a] Mattia Donzelli,[b] Herwig Requardt,[b] Christian Nemoz,[b] Marco Petasecca,[a] Elke Bräuer-Krisch,[b] Anatoly Rosenfeld[a] and Michael Lerch[a]

[a]Centre for Medical Radiation Physics, University of Wollongong, Australia, and [b]European Synchrotron Radiation Facility, France. *Correspondence e-mail: pauline.fournier.pf@gmail.com

Microbeam radiation therapy (MRT) is a novel irradiation technique for brain tumours treatment currently under development at the European Synchrotron Radiation Facility in Grenoble, France. The technique is based on the spatial fractionation of a highly brilliant synchrotron X-ray beam into an array of microbeams using a multi-slit collimator (MSC). After promising pre-clinical results, veterinary trials have recently commenced requiring the need for dedicated quality assurance (QA) procedures. The quality of MRT treatment demands reproducible and precise spatial fractionation of the incoming synchrotron beam. The intensity profile of the microbeams must also be quickly and quantitatively characterized prior to each treatment for comparison with that used for input to the dose-planning calculations. The Centre for Medical Radiation Physics (University of Wollongong, Australia) has developed an X-ray treatment monitoring system (X-Tream) which incorporates a high-spatial-resolution silicon strip detector (SSD) specifically designed for MRT. In-air measurements of the horizontal profile of the intrinsic microbeam X-ray field in order to determine the relative intensity of each microbeam are presented, and the alignment of the MSC is also assessed. The results show that the SSD is able to resolve individual microbeams which therefore provides invaluable QA of the horizontal field size and microbeam number and shape. They also demonstrate that the SSD used in the X-Tream system is very sensitive to any small misalignment of the MSC. In order to allow as rapid QA as possible, a fast alignment procedure of the SSD based on X-ray imaging with a low-intensity low-energy beam has been developed and is presented in this publication.

1. Introduction

Quality assurance (QA) in any radiotherapy modality is crucial to mitigate the risk of side-effects due to accidental over-dosage of healthy tissue, and maximize the efficacy of the treatment by ensuring adequate dose coverage to the target. Pre-treatment quality control (QC) is a vital link in the QA chain (IAEA, 2000) when combined with other routine QCs such as patient-specific independent pre-treatment dose calculations [Monte Carlo checking of treatment planning system (TPS) calculations] (Bush et al., 2011), in vivo dosimetry (Qi et al., 2011) and patient follow-up (Gehrmann et al., 2014).

For the past decade, patient-specific pre-treatment plan verification in conventional radiotherapy modalities such as intensity modulated radiation therapy (IMRT) and volumetric modulated arc therapy (VMAT) has mostly been carried out using two-dimensional dosimetry devices (Boggula et al., 2011) including, for small-field dosimetry, the recently introduced high-spatial-resolution 'MagicPlate-512' (Aldosari et al.,

Sensitive Volume

800 µm   10 µm
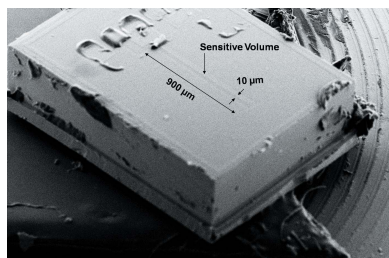
2014). These devices are embedded in a solid water phantom and subject to irradiation by each treatment field. The resulting two-dimensional dose distribution is then compared with that predicted by the TPS following calculation of the dose distribution in a virtual water volume. This comparison is typically carried out using gamma analysis: a hybrid distance-to-agreement/dose difference method (Low & Dempsey, 2003). Recently, the clinical relevance of performing such a comparison has been questioned as there is a lack of correlation between agreement of two-dimensional dose distributions measured and calculated in water and agreement between clinically relevant parameters such as dose-volume histograms (DVHs) in the patient anatomy (Zhen et al., 2011). As a result, there is a move towards fluence-based pre-treatment plan verification. In this revised approach, the fluence map of the treatment field is measured, used to calculate a three-dimensional dose distribution in a patient computed tomography dataset, and derive clinically relevant dosimetric quantities from DVHs (Nakaguchi et al., 2015). In this article we investigate the feasibility of applying such an approach to microbeam radiation therapy.

Microbeam radiation therapy (MRT) is an exciting development in the field of radiation oncology. It involves the treatment of tumours using planar arrays of highly collimated low-divergent X-ray microbeams. The underlying principle of MRT is a fascinating radiobiological effect known as the dose-volume effect, whereby healthy tissue demonstrates a remarkable resistance to ionizing radiation when spatial fractionation of the primary beam into microscopic beams is employed (Zeman et al., 1961). The fundamental cause for this difference in response, and the optimal level of spatial fractionation, is the topic of ongoing investigations (Dilmanian et al., 2002; Serduc et al., 2008, 2009; Bouchet et al., 2010, 2013, 2014, 2015; Sprung et al., 2012; Fernandez-Palomo et al., 2013). To date the majority of studies have been carried out at the European Synchrotron Radiation Facility (ESRF) and have shown the efficacy of MRT in treating gliomas in rats and mice (Laissue et al., 1998; Régnard et al., 2008; Serduc et al., 2008; Schültke et al., 2008; Bouchet et al., 2010, 2012). As a result, veterinary trials are commencing at the ESRF. Currently MRT is limited to synchrotron research facilities owing to the requirements for low-divergence and high-intensity X-ray sources; however, interest in hospital-based systems is growing (Hadsell et al., 2013).

The MRT lateral dose profile consists of a succession of peaks corresponding to the dose deposited by the microbeams. The dose deposited in the region between two peaks originates from the scattered photons from the peaks and is called the valley dose. The ratio between these two doses is an important parameter and is called peak-to-valley dose ratio (PVDR). In order to remain safe for the healthy tissue, the spatial beam fractionation needs to be ensured and the valley dose must remain below the organ dose tolerance (Dilmanian et al., 2002). Moreover, the MRT treatment is delivered in one single fraction. Consequently there is a pressing need for rapid and effective pre-treatment QA of the intensity distribution of MRT microbeams.

Gafchromic® films are currently the reference dosimeters for the peak and valley dose experimental determination in MRT and good agreement has been obtained between Gafchromic® films and Monte Carlo simulations for the determination of the PVDR (Martínez-Rovira et al., 2012; Bartzsch, 2014). However, a delay between 24 and 48 h is necessary between the film exposure and reading in order to allow the polymerization process to stabilize (Niroomand-Rad et al., 1998). Moreover, even films dedicated to high-doses measurements have dose range limitations that prevent the peak and valley dose to be read on the same film. The limited dynamic range of the film response combined with the large PVDRs typically utilized in MRT thus make precise dosimetry very challenging.

The Centre for Medical Radiation Physics (CMRP) has been working on dosimetry in MRT since 1996. MOSFET (metal oxide semiconductor field-effect transistor) detectors were the first solid-state dosimetry devices investigated due to their high spatial resolution (about 1 µm) and their ability to give an instant readout (Rosenfeld et al., 1999; Kaplan et al., 2000). They have been used for the measurements of peak dose, valley dose and PVDRs at the ESRF (Bräuer-Krisch et al., 2003; Siegbahn et al., 2009). However, the MOSFET detectors had a low tolerance to high dose rates that prevented them from being used under the full beam intensity conditions under which MRT is performed. Indeed, Siegbahn et al. (2009) observed that the MOSFET was saturated after an accumulated absorbed dose of 1000 Gy and had to be replaced. This composes a major limitation of the device since dose rates as high as 20 kGy s^{-1} can be encountered in MRT. Moreover, it has also been stated that the interaction of the microbeam with the different average atomic number of the elements composing the MOSFET detector induced a lateral distortion in the microbeam profile (Rosenfeld et al., 2005). The CMRP thus developed a new dosimetry system for MRT applications based on a high-resolution single strip detector (SSD) (Lerch et al., 2011; Petasecca et al., 2012).

At the ESRF, the alignment of the multi-slit collimator (MSC) is performed by monitoring the output of a downstream large-area ionization chamber (IC), covering the whole beam, while rotating the MSC about its vertical axis. The MSC is considered to be optimally aligned when the integrated air-kerma measured by the IC is maximum. However, the IC is not able to provide any information regarding the intensity profile of the microbeams. Herein we investigate the ability of the SSD to detect minute misalignment of the MRT MSC, and its potential use for rapid pre-treatment quality assurance in MRT.

2. Material and methods

2.1. ID17 MRT beamline

The ID17 MRT beamline has been described in numerous publications, with detailed descriptions given by Martínez-Rovira et al. (2012) and Cornelius et al. (2014). The beamline is located at the ESRF, a third-generation synchrotron source,

where high-intensity low-divergent X-rays are generated *via* a wiggler insertion device. For MRT irradiations, the wiggler gap is set to its minimum value of 24.8 mm. Several absorbers downstream from the wiggler are used to remove the low-energy components from the white-beam spectrum and the MSC is included in the beam path to generate the microbeams. The resulting spectrum corresponds to the pre-clinical beam filtering conditions and has a mean energy of 105 keV (Crosbie *et al.*, 2015).

For the in-air experiment presented in this publication, two additional beam modifiers were inserted in the beam; a krypton gas filter (Requardt *et al.*, 2013) and two redundant Compton chambers (Berkvens *et al.*, 2013). Both devices are used in the context of the veterinary trials for patient safety purposes. At a 24.8 mm wiggler gap, the insertion of these additional elements shifts the mean energy from 105 to 108 keV.

In the current study, the most relevant beamline components are the beam-defining vertical slits, horizontal slits, the high-precision MSC and the goniometer. The horizontal slits are oxygen-free copper blocks situated at around 29.3 m from the source and define the horizontal limits of the beam at the patient position. A reference lateral field size in MRT of 20 mm was used in this study. The vertical slits, located at 38.8 m from the source, comprise tungsten carbide blocks with an aperture of 500 μm, resulting in a beam height of 520 μm at the patient position due to beam divergence. The MSC is positioned at 39.3 m from the source and consists of a 8 mm-thick block of tungsten carbide inside which 50 μm-wide slits have been created using a high-precision wire-cutting technique (Bräuer-Krisch *et al.*, 2009). The MSC thus produces 50 μm FWHM microbeams separated by a centre-to-centre (c-t-c) distance of 400 μm. The patient, or dosimetry phantom, is installed on a Kappa-type goniometer (Huber, Germany) for positioning. Owing to the limited beam height, the goniometer is used to scan the patient/phantom through the MRT field in order to cover larger tumour sizes.

2.2. Detector and readout

The SSD used in the current study is an epitaxial device fabricated by SPA BIT (Ukraine) whose sensitive volume (SV) consists of a single silicon microstrip. A 50 μm-thick epitaxial substrate is grown on top of a 370 μm-thick layer of lower resistivity (Lerch *et al.*, 2011; Petasecca *et al.*, 2012) and the SV of 900 μm × 10 μm is achieved *via* ion implanation. Scanning electron microscopy (SEM) images of the detector have been acquired at the ESRF in order to observe the SSD main features and to verify their dimensions. On the SEM image displayed in Fig. 1, one can easily distinguish the SSD sensitive volume.
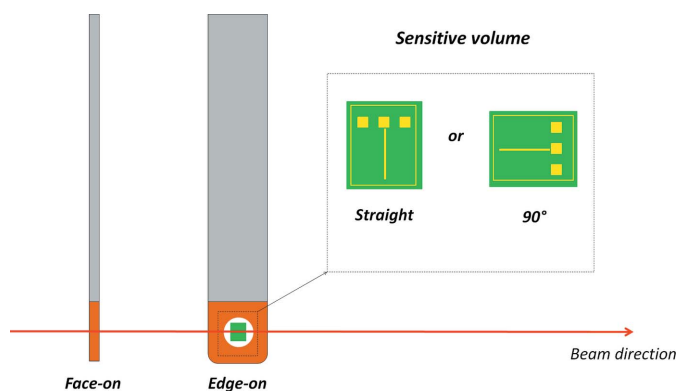
Because of the very small dimension of the SV, very high spatial resolution dosimetry can be performed by using detectors in the 'edge-on' configuration; *i.e.* with the normal to the surface of the detector orthogonal to the beam direction (see Fig. 2). Indeed, when used in this orientation, the effective spatial resolution of the detector is mostly defined by the
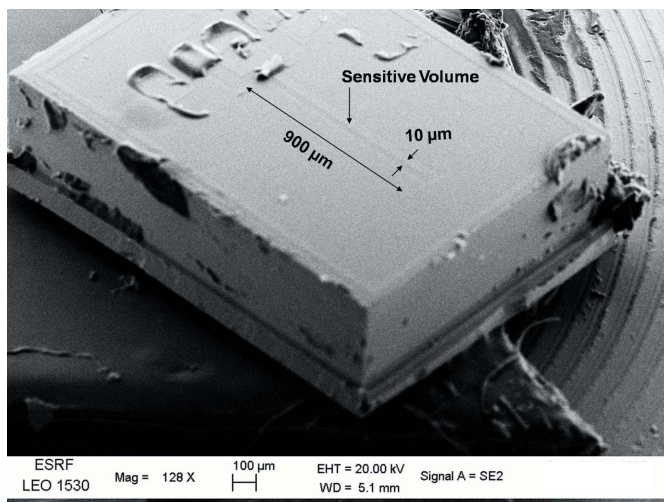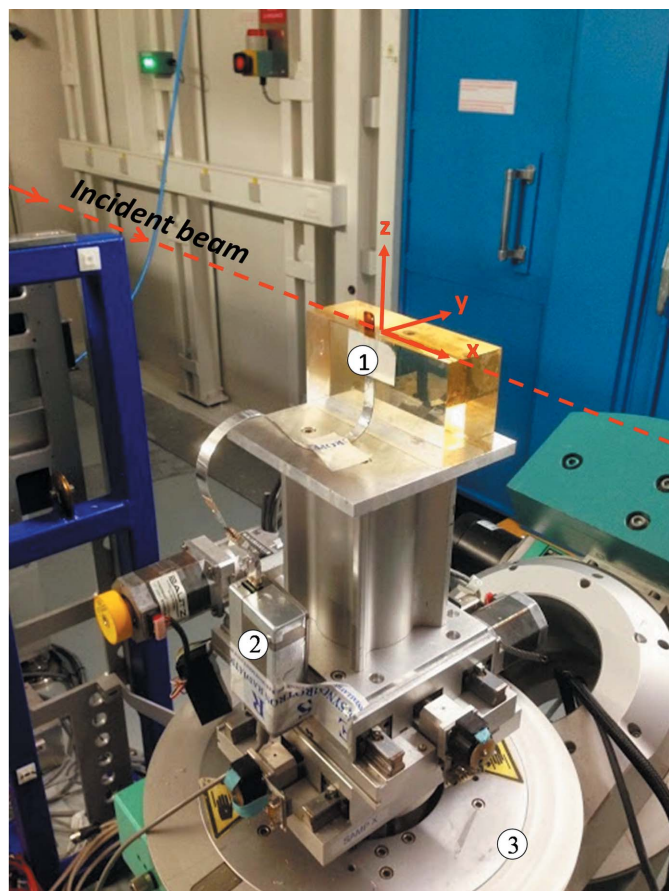

Figure 1
SEM image of the SSD chip where the 900 μm × 10 μm sensitive volume is indicated.

depletion length and, owing to the low resistivity of the silicon, can be as low as 10–12 μm for an applied bias of −30 V (Petasecca *et al.*, 2012). Two orientations of the SV are available. In the edge-on configuration, the so-called '90°' orientation has the long axis of the SV strip parallel to the beam direction. Conversely, the so-called 'straight' orientation has the long axis of the SV strip orthogonal to the beam in the vertical direction. The different possible orientations of the detector and of the SV are illustrated in Fig. 2.

Horizontal detector response profile measurements were performed in air. In this situation the X-rays interacting in the packaged silicon device lead to a photocurrent. This current is sampled and recorded using a fast data acquisition system as described in detail by Petasecca *et al.* (2012). The data acquisition system includes a pre-amplifier module that converts the currents from nano-Ampere to ADC (analogue to digital converter) counts (arbitrary units). In the current study, the pre-amplifier had a conversion factor equal to 0.543 counts nA^{-1}. The custom software *RADPLOT* is used

Figure 2
Diagram explaining the different possible orientations of the SSD relative to the beam (face-on or edge-on) as well as the two different possible orientations of the sensitive volume (straight or 90°).

The imaging system comprises a two-dimensional X-ray detector located around 4.3 m downstream of the goniometer stage. The detector consists of a Fast-Readout Low-Noise CCD camera (FReLoN) developed at the ESRF (Labiche *et al.*, 2007). A characterization of the FReLoN camera is given by Coan *et al.* (2006). The aim is to benefit from the small pixel size (23.26 µm × 23.26 µm at the sample stage) of the FReLoN camera to image the SSD chip in order to align it with the beam.

When switching from irradiation to imaging mode, the beam-defining slits can be removed from the beam path leading to a beam height of around 2 mm at the goniometer stage. For large samples, in order to avoid the limitation of the image dimension in the vertical direction, a vertical scan is performed using the goniometer and images are acquired at different vertical offsets. The acquired frames are piled up together to obtain a complete image of the sample (Serduc *et al.*, 2010).

During the beam alignment procedure, the pixel of the FReLoN camera corresponding to the central part of the beam is defined as the central pixel. When the MSC is inserted in the beam, the plane of the resulting X-ray microbeams is parallel with the vertical plane of the FReLoN camera (see Fig. 4). The MSC is aligned in the beam in order to make the centroid of the central microbeam match with the central pixel of the camera.

To proceed to the SSD imaging, the detector was set up on the goniometer stage and the MSC removed from the beam path. One frame image of the SSD was acquired by exposing the detector for 0.1 s. On the resulting image, the vertical and horizontal offset between the current position of the centre of the SSD chip and the central pixel position can be quantified. The detector was thus moved to the central position using the goniometer vertical and horizontal motion motors. A second image is usually acquired to verify its correct alignment.

2.4. QC of multi-slit collimator alignment

At the ID17 biomedical beamline of the ESRF, the MSC is aligned by the monitoring of the output of a beam monitor IC whilst rotating the MSC about the vertical axis (z) perpendicular to beam direction (x). The MSC is rotated through small angles, typically ranging from 0.1° to −0.1° in increments of 0.01°. During alignment, the wiggler gap is set to a nominal setting of 40 mm in order to minimize beam fluence and associated ozone accumulation in the experimental hutch. In order to benchmark SSD measurements against the IC, the measurements with the SSD were also performed for a wiggler gap of 40 mm. For the beam filtering conditions considered

Figure 3
Photograph of the setup used for the in-air experiment. (1) SSD oriented edge-on; (2) pre-amplifier module; (3) goniometer stage.

to configure the data acquisition system, acquire data and display the ADC counts against time profile. After careful alignment of the device with the central axis of the synchrotron radiation beam, and by scanning the device in the horizontal direction, one is able to measure the energy deposition in silicon in the array of microbeams. To facilitate rapid installation, alignment and scanning, the device was mounted directly on the goniometer stage in an in-air configuration (see Fig. 3). The advantage of this method is that the QA procedure is fast; however, no dosimetry measurements can be performed due to the lack of scattering material surrounding the sensitive volume of the detector. This is the reason why all SSD results obtained using this method are presented in terms of ADC counts.

2.3. Rapid detector alignment using pink-beam imaging

An imaging modality known as 'pink-beam' imaging (Serduc *et al.*, 2010) was used to align the device with the beam axis. Currently, the imaging beam is obtained by opening the wiggler gap from 24.8 mm to 100 mm and removing the MSC from the beam path. Under pre-clinical beam filtering conditions, moving from the irradiation to imaging modality decreases the beam intensity by 99.99% and shifts the mean energy from the initial 105 keV to 50 keV.

during the experiments, moving the wiggler gap from 24.8 to 40 mm led to 62% photon flux decrease and moved the mean energy from 108 to 90 keV.

We used here a SSD with a straight orientation of the SV and the detector was oriented edge-on. The straight orientation of the SV was chosen to minimize the misalignment of the SV with the microbeams. The MSC rotation angle was moved between $0.05°$ and $-0.05°$. For each angle, the SSD was horizontally scanned through the 2 cm large array of microbeams at a constant speed ($2\ \text{mm s}^{-1}$). As the measurements were performed in air, the notion of PVDR is irrelevant in the context of the present study. We thus introduced the notion of peak-to-valley intensity ratio (PVIR) corresponding to the peak signal divided by the valley signal measured by the SSD. The effect of the MSC rotation on the peak and valley signal, PVIR and shape of the microbeams was investigated.

Figure 6
A 2 cm-wide array of microbeams acquired in air with the SSD (after substraction of the baseline) for a wiggler gap of 40 mm. MSC rotation angle = $0°$.
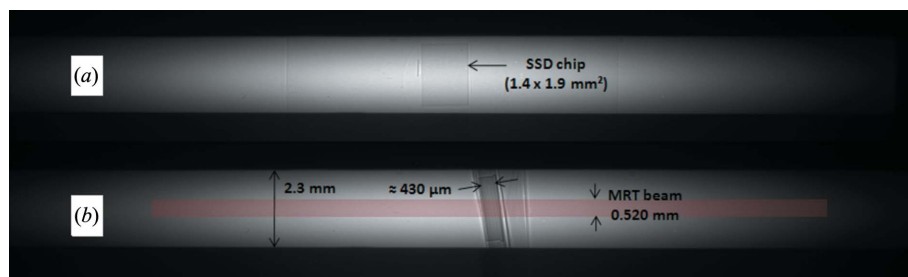
3. Results

3.1. Rapid detector alignment with pink-beam imaging

The images acquired during the alignment process for both face-on and edge-on detector orientations are displayed in Fig. 5. These images consist of one single frame acquisition (*i.e.* the SSD was not moved through the beam during the image acquisition, only one image was acquired at a given vertical position of the detector).
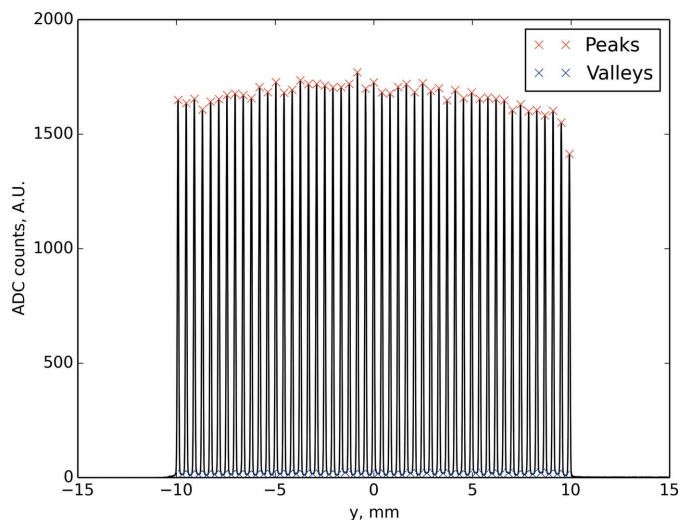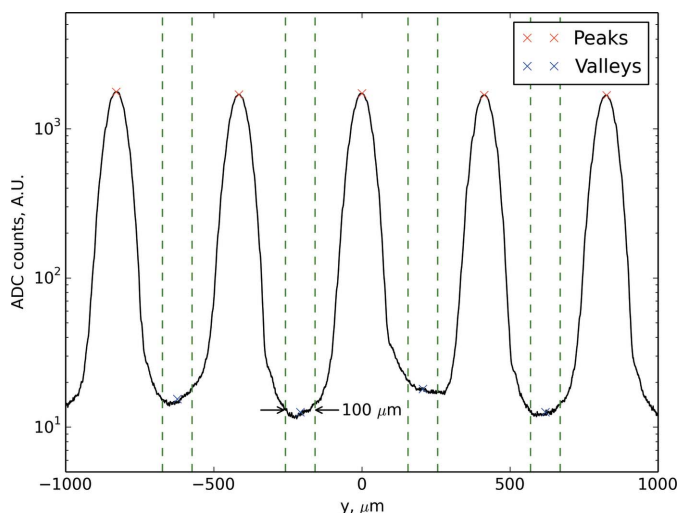
The pink-beam imaging of the detector is very fast as a 0.1 s exposure per frame was sufficient to acquire the image of the detector with a satisfying image quality. Therefore, the total time to set up the detector and align it in the centre of the beam was approximately 30 min.

In clinical practice a pre-aligned SSD could be mounted permanently in air. The imaging procedure would thus merely confirm that no misaligment of the detector, with respect to the microbeams, had occurred immediately prior to exposing the SSD to the full intensity X-ray microbeams to characterize the intrinsic MRT field profile.

The red area on the image represents the height of the MRT beam used for the experiment (*i.e.* 520 µm high at the goniometer stage). One can notice that only a part of the detector

was exposed by the beam as the sensitive volume of the SSD (900 µm) is longer than the beam height.

3.2. QC of the multi-slit collimator alignment

The *RADPLOT* software records the ADC counts as a function of time. Knowing the scan speed of the motor used to perform the acquisition of the microbeams horizontal profile, we are able to convert the time variable into a distance value. The detector response profile of a 2 cm-wide array of X-ray microbeams obtained for a $0°$ angle of the MSC is displayed in Fig. 6. In this figure, the *RADPLOT* data have been averaged by a factor equal to 500 and the baseline signal has been subtracted. During the experiment, the baseline noise of X-Tream with the SSD was better than ± 1.3 ADC counts (one standard deviation) with no averaging applied. In Fig. 6 we can verify the dimension of the lateral field size and that all 49 microbeams are correctly present. The peak and valley signals are also presented on this figure by red and blue crosses, respectively. The peak signal is defined as the maximum signal in the microbeam.

Fig. 7 presents a focus on the five central microbeams of the array presented in Fig. 6. As a logarithm scale is used on the ordinate axis, one can notice that the valley is not stable and the lowest value is not necessary in the middle of two consecutive microbeams. Therefore, in order to determine the valley signal, the signal has been averaged over a region of interest of 100 µm centred in the middle of two consecutive microbeams. The resulting valley is presented by the blue crosses in Fig. 7.
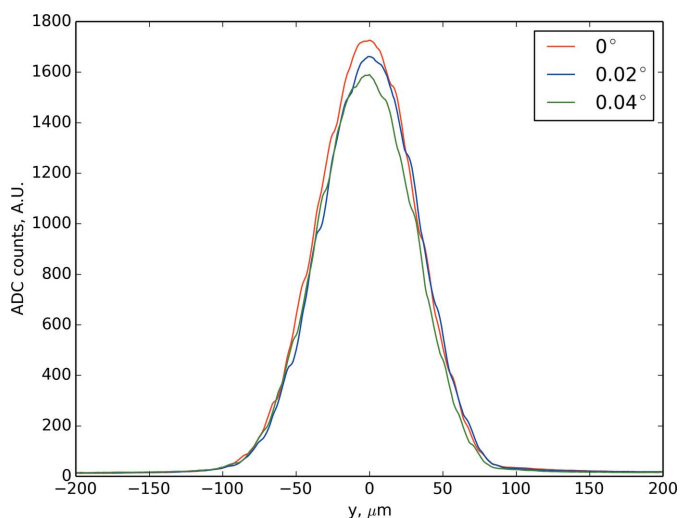
Fig. 8 represents the central microbeam profile obtained for $0.0°$,

Figure 5
Images of the detector chip acquired with the FReLoN camera, in (*a*) face-on and (*b*) egde-on orientation, with one single frame and 0.1 s exposure. The red area on the image represents the dimensions of the MRT beam used for the experiment (*i.e.* 520 µm high at the goniometer stage).
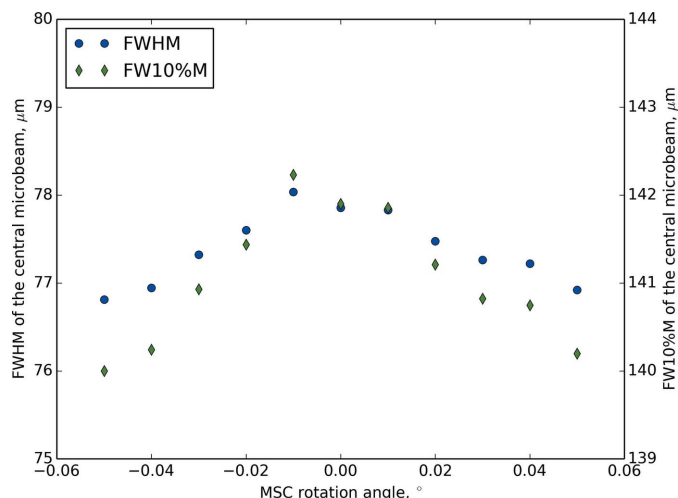
Figure 7
Focus on the five central microbeams of the 2 cm-wide array of microbeams acquired in air with the SSD for a wiggler gap of 40 mm. MSC rotation angle = 0°.

Figure 9
FWHM and FW10%M of the central microbeam as a function of the MSC angle. Only a 1.6% decrease is observed between the highest and lowest FWHM and FW10%M values.

0.02° and 0.04° rotation angle of the MSC about the z-axis. One can see that the intensity of the central microbeam is decreasing with the MSC angle because of the reduced aperture resulting from the MSC misalignment.

With the change of the MSC rotation angle, one would expect the full width at half-maximum (FWHM) of the central microbeam to decrease as the effective slit aperture is decreasing. Consequently, one possible way to check the MSC alignment would be to measure the FWHM of the central microbeam for the different angles of rotation investigated. The highest FWHM should then be obtained for a rotation angle corresponding to the optimum alignment of the MSC. For the different angles of rotation investigated, the lateral profile of the central microbeam has thus been fitted with a Gaussian (not shown here) in order to extract the FWHM and FW10%M (full width at 10%-maximum) values from the

fitting equation. The resulting FWHM and FW10%M values are reported in Fig. 9. Only a 1.6% decrease is observed between the highest and lowest FWHM and FW10%M values which highlights the advantage of rather using an intensity method to determine the optimum MSC rotation angle.

At the ESRF, the readings from a monitoring IC are used for MSC alignment purposes by acquiring the IC signal while rotating the MSC. The maximum integrated air kerma (proportional to the total fluence) measured by the IC is considered to correspond to the optimum MSC alignment with the beam. However, no information about the intensity of each microbeam can be obtained from the IC. From the horizontal profiles obtained in-air with the SSD, the integrated counts over the resulting microbeam arrays have been extracted for each MSC rotation angle investigated. Fig. 10 compares the monitoring IC signal recorded for MSC rotation

Figure 8
Central microbeam signal for three different rotation angles of the MSC (0°, 0.02° and 0.04°).
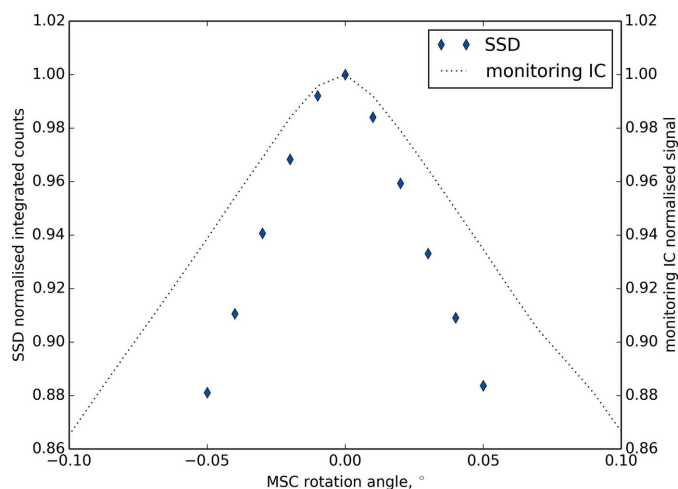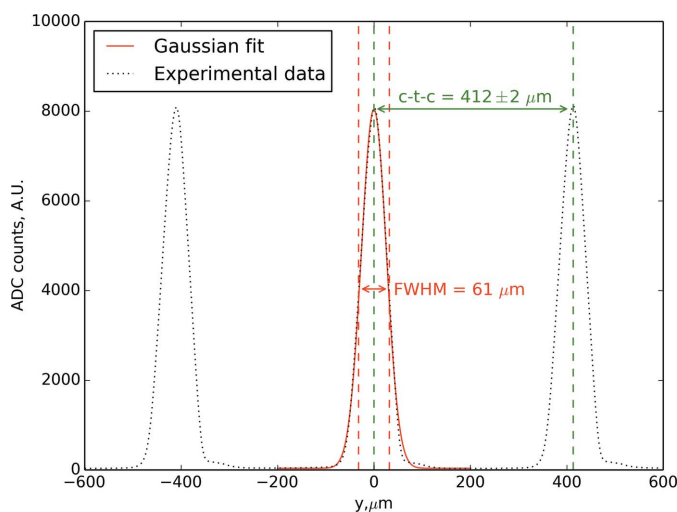

Figure 10
Total silicon SSD counts integrated over the microbeam array for the different angles investigated and comparison with the results obtained by the beam-monitoring IC.
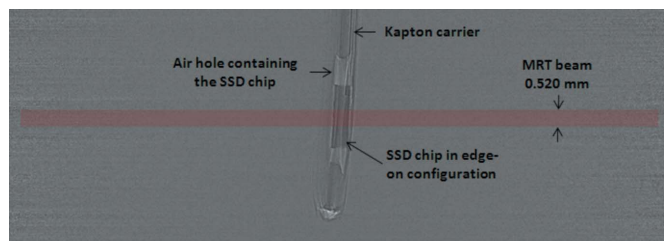
research papers

angles ranging from −0.1° to 0.1° with the integrated count values extracted from the SSD measurements. Each set of data is normalized to 1 for their respective maximum recorded value. A good correlation can be established between the two detectors as they both agree on a maximum signal reached for 0°.

From Fig. 9 one can see that, for a 0.0° rotation of the MSC, the FWHM of the central microbeams is around 78 μm. At the goniometer stage, the microbeam FWHM is expected to be equal to 51.5 μm due to the beam divergence. The over-estimation of the microbeam width is due to misalignment of the SV of the detector. Indeed, the SV length should be parallel to the microbeams but, as one can see in Fig. 5(b), the SSD chip is slightly tilted in the vertical direction (∼7°) which degrades the effective spatial resolution.

A lateral profile containing 49 microbeams has been acquired with the SSD fixed at 2 cm depth in a phantom made of water equivalent material. For these measurements, the krypton gas filter and the two redundant Compton chambers were kept out of the beam leading to an increase of 25% of the beam intensity compared with the previous experiments. The wiggler gap was set to 40 mm. The three central microbeams of the resulting array are displayed in Fig. 11 and the central microbeam is fitted with a Gaussian. As the SSD was rigidly mounted in the edge-on orientation in the phantom, it was thus less sensitive to motion and its alignment could be performed with a higher accuracy. Indeed Fig. 12 shows the pink-beam image acquired during the SSD alignment within the water equivalent phantom and one can clearly notice that the tilt of the SSD chip (∼3°) has been reduced compared with the in-air configuration. The spatial resolution has thus been improved accordingly: in Fig. 11 the FWHM of the central microbeam, deduced from the Gaussian fitting equation, is equal to 61 μm. It should be noted that all FWHM values reported in this study include the intrinsic dimensions of the SSD.
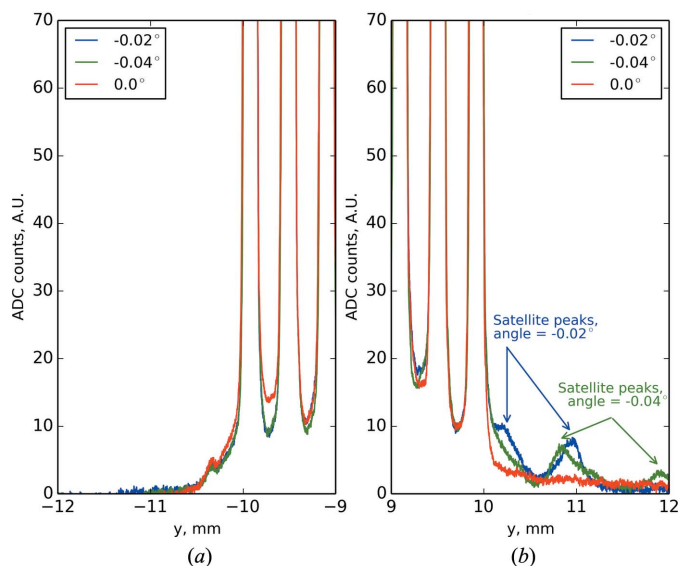

Figure 12
Image of the SSD rigidly fixed in the edge-on orientation within a water equivalent phantom acquired with the FReLoN camera. The red area in the image represents the dimensions of the MRT beam used for the experiments (i.e. 20 mm × 520 μm at the goniometer stage).

Concerning the c-t-c distance, a value of 412 ± 2 μm was measured in the water equivalent phantom and 413 ± 2 μm in air. These values are in close agreement with the 412.2 ± 3.2 μm c-t-c distance reported by Bräuer-Krisch et al. (2009) from Gafchromic® films measurements and with the 412.2 μm expected value at the goniometer stage due to the beam divergence.

3.3. Effect of the MSC rotation angle on the intensity distribution of microbeams

When performing measurements for the QA of the MSC alignment, we observed satellite peaks on the edge of the array of microbeams for small rotation angles of the MSC. Fig. 13 compares the SSD response profile on the field edges for three different angles: 0.0°, −0.02° and −0.04°. Satellite peaks are only present on the right-hand edge of the array of microbeams when the MSC is misaligned. Conversely, for positive angles of rotation of the MSC, satellite peaks only appear on the left-hand edge of the array of microbeams (see

Figure 11
Central microbeams signal obtained at 2 cm depth in a water equivalent phantom. The krypton gas filter and the two redundant Compton chambers were out of the beam. The wiggler gap was set to 40 mm.

Figure 13
Left (a) and right (b) edges of the microbeams array profile for 0°, −0.02° and −0.04° rotation angles of the MSC. For negative rotation angles of the MSC, satellite peaks appear on the right edge of the array of microbeams.
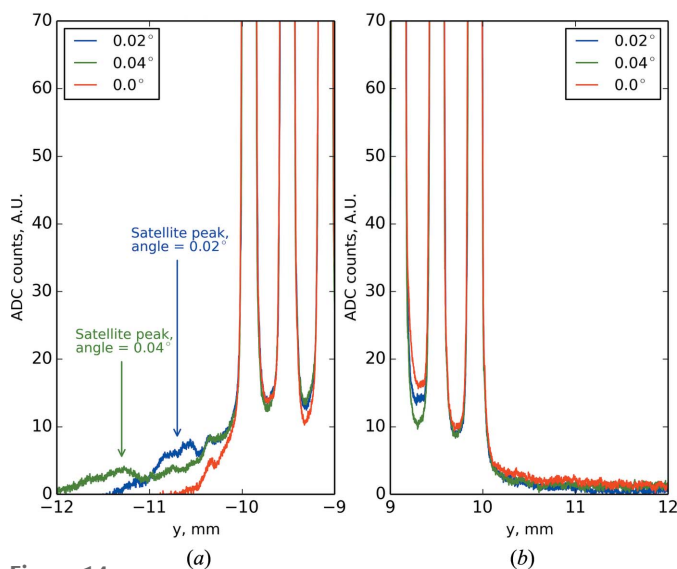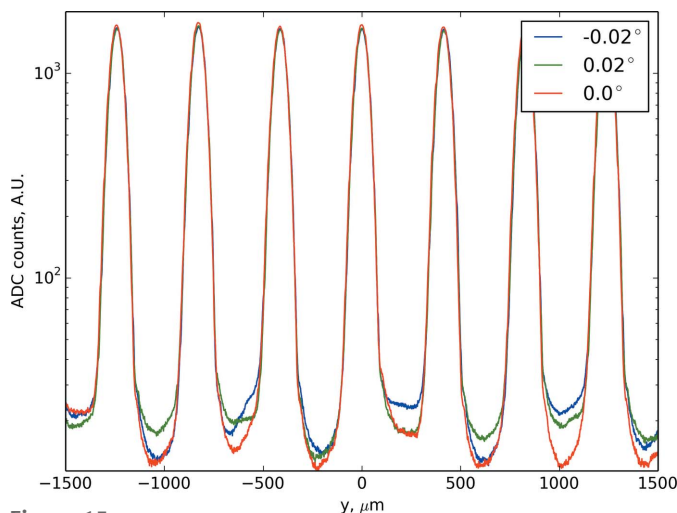
Figure 14
Left (*a*) and right (*b*) edges of the microbeams array profile for 0°, 0.02° and 0.04° rotation angles of the MSC. For positive rotation angles of the MSC, satellite peaks appear on the left edge on the array of microbeams.

Fig. 14). As the satellite peaks are only observed on one side of the array and as this side is dependent on the direction of rotation of the MSC, they are likely to be related to total external reflection of the photons on the side walls of the MSC. This represents an important finding, as the detection of satellite peaks suggests a dose deposition outside of the irradiation field and must be minimized.

As we observed the effect of the misalignment of the MSC on the edges of the microbeams array, Fig. 15 shows the effect induced on the central microbeams for the following MSC rotation angle: −0.02°, 0° and 0.02°. One can see that the MSC rotation angle has a strong influence on the valley signal. Once again, photon reflections may occur on the side walls of the MSC and modify the valley dose.

Fig. 16 displays the average of the 48 peaks and 48 valley signals measured over the array of microbeams as a function

Figure 15
Central microbeams obtained for three different rotation angles of the MSC (−0.02°, 0° and 0.02°).
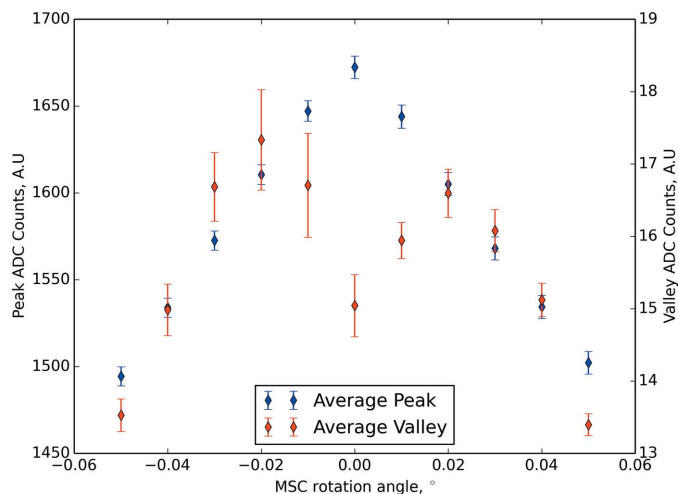
Figure 16
Average peak and valley signals obtained for the full range of angles investigated.

of the MSC angle. The uncertainty bars represent the standard deviation of the mean σ_{mean}, defined as

$$\sigma_{\text{mean}} = \frac{\sigma}{\sqrt{N}} = \frac{1}{\sqrt{N}}\left[\frac{1}{N-1}\sum_{i=1}^{N}(x_i - \bar{x})^2\right]^{1/2}, \qquad (1)$$

where N is the number of peaks or valleys measured in one array of microbeams (48 in the present case) and $\bar{x}$ is either the peak or valley mean value over the array of microbeams. The valley signal first increases with rotation angle of the MSC, from 15 counts at 0° to around 17 counts at ±0.02°. For larger angles, the signal in the valley decreases due to the higher effective thickness of the MSC with misalignment thus attenuating even more the primary beam. For the peaks, the signal decreases constantly with the MSC angle as previously observed in Fig. 8.

As measurements were performed in air, the SSD should ideally only be sensitive to the photon flux. At the centre of the microbeam the flux is not expected to change significantly for such small MRT collimator angles since the air-scatter contribution to the photon flux here is negligible. The immediate decrease in response to angle demonstrates that the SSD is sampling the intensity across a significant proportion of the width of the microbeam. This result is consistent with the SSD effective spatial resolution degradation observed when the SSD is misaligned.

The 48 PVIR values deduced from the peak and valley signals measurements over the microbeam array have been averaged and are presented in Fig. 17 as a function of the MSC rotation angle. The error bars represent the standard deviation of the mean. For rotation angles between 0 and ±0.02°, the PVIR decreases as the peak signal is decreasing while the valley signal is increasing. For larger angles, the PVIR increases again as the valley signal decreases at a higher rate than the peak signal.

The QA results presented here highlight the importance of precise alignment of the MSC relative to the X-ray beam. Even in what may be considered a worst-case scenario for the
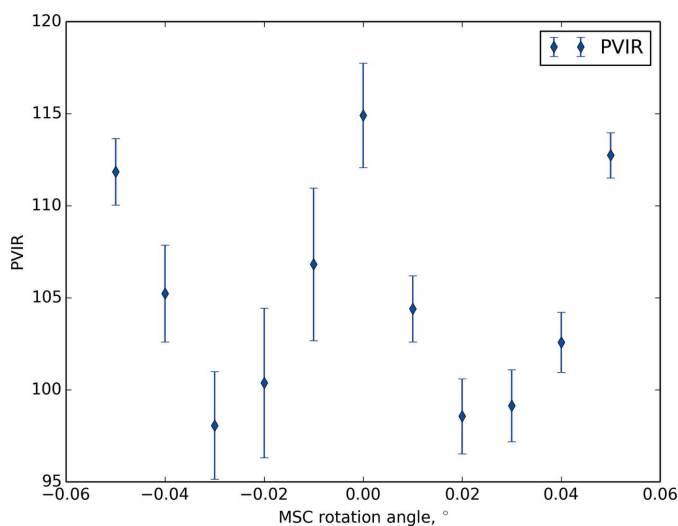
Figure 17
Average PVIRs obtained for the full range of angles investigated.

SSD (poorly aligned), the system is still able to confirm that the MSC is aligned appropriately. However, in order to precisely determine the relative peak intensity of each microbeam for input into the dose-planning system the SSD should be optimally aligned.

4. Discussion

A single silicon-based strip detector was used for the acquisition of one-dimensional profiles in air of the synchrotron beam used in MRT. The SSD was used to measure the horizontal profiles of a 2 cm-wide microbeam array. The detector was able to detect small misalignments of the MSC which resulted in changes in the valley shape but also in modifications of the peak, valley and PVIR values. The rotation of the MSC did not have a significant impact on the FWHM and FW10%M values extracted from the Gaussian fit of the central microbeam of the array under the measurements conditions presently used. The significance may increase if the detector had a spatial resolution of 1 µm and was perfectly aligned with the X-ray microbeams. Such a detector is under development and will therefore be investigated in the future. Consequently, the MSC alignment was performed by calculating the integrated counts recorded over the array of microbeams by the SSD for the different rotation angles of the MSC. The results were in agreement with the monitoring IC currently used for the MSC alignment on ID17.

The SSD provided a complete view of the microbeam array enabling rapid verification of the lateral field size as well as the correct shape and number of microbeams. As the alignment of such a small device can be tedious, we have developed an alignment procedure based on the pink-beam imaging modality available at the ESRF, allowing an alignment of the SSD within half an hour for a completely dismantled SSD.

Using the SSD, satellite peaks have been detected outside of the defined irradiation field for a misalignment angle of the MSC as small as −0.02°. The presence of such peaks suggests that additional energy depositions could occur in the regions between the microbeams, and this will be the subject of a separate dosimetry investigation in the future. These satellite peaks originate from photons that have undergone total external reflection from the inner surface of the MSC. Future Monte Carlo studies interfaced with a ray-tracing and X-ray optics code (Cornelius et al., 2014) should be conducted in order to validate this hypothesis. If this is the case, one way to alleviate this problem would be to adapt the MSC aperture to the beam divergence in order to have an angle of incidence greater than the critical angle to prevent total external reflection from occurring. Pre-treatment QA using the SSD could thus be performed to ensure that the MSC is accurately aligned and that the treatment beam profile is clear of any satellite peaks.

The scattering of photons into the valley regions between two microbeams is very sensitive to any changes in the irradiation set-up, in particular to the alignment of the MSC. Such scattering should be avoided if possible or at least well characterized as the scattered photons will lead to an increase in the valley dose which could compromise the sparing of the normal tissue. Dedicated measurements to ensure patient safety should therefore additionally be performed with the SSD in the future.

On the horizontal scan of the 2 cm-wide microbeam array acquired, the measured c-t-c distance was in very good agreement with the values previously reported by Bräuer-Krisch et al. (2009). However, an over-estimation of the microbeam width was observed and attributed to a slight misalignment of the detector.

Indeed, the greatest limitation highlighted in this study is the degradation of spatial resolution when the SV is not perfectly aligned with the beam axis. The angular misalignment of the detector could be mitigated using an additional positioning motor available on the goniometer. However, using such motors requires the SSD to be precisely positioned at the centre of rotation of the goniometer coordinate frame of reference. Adding the alignment of the SSD on the rotation axis of the goniometer as a step within the detector set-up would lead to a much more time-consuming task. A decrease in the SV length could be considered to mitigate for the detector sensitivity to slight misalignments. However, the dimensions of the SSD must be designed in such a way so as to ensure that an adequate photocurrent is able to be generated in all MRT dosimetry and QA conditions (microbeam peak and valley regions, beam filtering, depth in water or water equivalent materials etc.). In addition, for ideal QA measurements one needs to minimize any partial volume effects related to the sensitive volume. Therefore a trade-off exists between SSD sensitivity and spatial resolution. A permanently mounted SSD in air, pre-aligned with the MRT beam, would consequently be the most suitable alternative. This solution will mean that the alignment will only need to be checked. In the future, it could be envisaged to perform a one-dimensional scan of the beam using a high-resolution one-dimensional array of silicon microstrip detectors which could provide an instantaneous one-dimensional fluence profile (Povoli et al., 2015). Another possible technical improvement

would be to include a modality within the *RADPLOT* software taking the motor scanning speed as an input and thus allowing the SSD signal to be displayed as a function of the distance. This would considerably facilitate and accelerate MRT QA procedures performed using the X-Tream system.

In the future, if the SSD is to be used as dosimeter in a clinical context, the SSD would be considered as single-use or disposable dosimeter and QA measurements could be performed within a water or solid water phantom. The SSD readings will have to be converted into absorbed dose values by calibrating the SSD using an ionization chamber under MRT reference dosimetry conditions as described by Bräuer-Krisch *et al.* (2015). For purely scientific studies and pre-clinical measurements, we will need to evaluate the SSD radiation lifetime by investigating the change in SSD response with total accumulated dose. This will be part of the standard scientific research operating procedures in order to ensure accurate and reproducible results from the SSD.

5. Conclusion

MRT represents important challenges in QA because of the strong influence in biological outcome from possible misalignment directly influencing the quality of the microbeams. QA in radiotherapy is required to ensure effective treatment and patient safety and an interest is rising in conventional radiotherapy to pursue fluence-based pre-treatment plan verification over in-phantom dosimetry measurements (Boggula *et al.*, 2010). The SSD, or similar technology, could be a potential candidate in the field of MRT to ensure that fluence profiles assumed by the TPS are consistent with response profiles experimentally acquired. Finally, one can consider extending the SSD use to MRT pre-clinical experiments where an accurate knowledge of the beam properties would contribute to reduce experimental uncertainties between two sets of experiments. Future work will concentrate on utilizing the SSD in a dosimetry study performed in a solid water phantom to investigate how the satellite peaks observed in this work translate into MRT dose profile measurements and the impact on the corresponding peak and valley dose.

Acknowledgements

References

Aldosari, A., Petasecca, M., Espinoza, A., Newall, M., Fuduli, I., Porumb, C., Alshaikh, S., Alrowaili, Z., Weaver, M., Metcalfe, P., Carolan, M., Lerch, M. L. F., Perevertaylo, V. & Rosenfeld, A. B. (2014). *Med. Phys.* **41**, 091707.

Bartzsch, S. (2014). PhD thesis, Heidelberg, Germany.

Berkvens, P., Brauer-Krisch, E., Brochard, T., Nemoz, C., Renier, M., Fournier, P., Requardt, H. & Kocsis, M. (2013). *Nuclear Science Symposium and Medical Imaging Conference (NSS/MIC) 2013*, pp. 1–3. IEEE.

Boggula, R., Birkner, M., Lohr, F., Steil, V., Wenz, F. & Wertz, H. (2011). *Phys. Med. Biol.* **56**, 7163–7177.

Boggula, R., Lorenz, F., Mueller, L., Birkner, M., Wertz, H., Stieler, F., Steil, V., Lohr, F. & Wenz, F. (2010). *Phys. Med. Biol.* **55**, 5619–5633.

Bouchet, A., Boumendjel, A., Khalil, E., Serduc, R., Bräuer, E., Siegbahn, E. A., Laissue, J. A. & Boutonnat, J. (2012). *J. Synchrotron Rad.* **19**, 478–482.

Bouchet, A., Lemasson, B., Christen, T., Potez, M., Rome, C., Coquery, N., Le Clec'h, C., Moisan, A., Bräuer-Krisch, E., Leduc, G., Rémy, C., Laissue, J. A., Barbier, E. L., Brun, E. & Serduc, R. (2013). *Radiother. Oncol.* **108**, 143–148.

Bouchet, A., Lemasson, B., Le Duc, G., Maisin, C., Bräuer-Krisch, E., Siegbahn, E. A., Renaud, L., Khalil, E., Rémy, C., Poillot, C., Bravin, A., Laissue, J. A., Barbier, E. L. & Serduc, R. (2010). *Int. J. Radiat. Oncol. Biol. Phys.* **78**, 1503–1512.

Bouchet, A., Sakakini, N., Atifi, M. E., Clec'h, C., Bräuer-Krisch, E., Rogalev, L., Laissue, J. A., Rihet, P., Le Duc, G. & Pelletier, L. (2014). *Intl J. Cancer*, **136**, 2705–2716.

Bouchet, A., Serduc, R., Laissue, J. A. & Djonov, V. (2015). *Phys. Med.* **31**, 634–641.

Bräuer-Krisch, E., Adam, J.-F., Alagoz, E., Bartzsch, S., Crosbie, J., DeWagter, C., Dipuglia, A., Donzelli, M., Doran, S., Fournier, P., Kalef-Ezra, J., Kock, A., Lerch, M., McErlean, C., Oelfke, U., Olko, P., Petasecca, M., Povoli, M., Rosenfeld, A., Siegbahn, E. A., Sporea, D. & Stugu, B. (2015). *Phys. Med.* **31**, 568–583.

Bräuer-Krisch, E., Bravin, A., Lerch, M., Rosenfeld, A., Stepanek, J., Di Michiel, M. & Laissue, J. (2003). *Med. Phys.* **30**, 583–589.

Bräuer-Krisch, E., Requardt, H., Brochard, T., Berruyer, G., Renier, M., Laissue, J. & Bravin, A. (2009). *Rev. Sci. Instrum.* **80**, 074301.

Bush, K., Gagne, I., Zavgorodni, S., Ansbacher, W. & Beckham, W. (2011). *Med. Phys.* **38**, 2208–2221.

Coan, P., Peterzol, A., Fiedler, S., Ponchut, C., Labiche, J. C. & Bravin, A. (2006). *J. Synchrotron Rad.* **13**, 260–270.

Cornelius, I., Guatelli, S., Fournier, P., Crosbie, J. C., Sanchez del Rio, M., Bräuer-Krisch, E., Rosenfeld, A. & Lerch, M. (2014). *J. Synchrotron Rad.* **21**, 518–528.

Crosbie, J. C., Fournier, P., Bartzsch, S., Donzelli, M., Cornelius, I., Stevenson, A. W., Requardt, H. & Bräuer-Krisch, E. (2015). *J. Synchrotron Rad.* **22**, 1035–1041.

Dilmanian, F. A., Button, T. M., Le Duc, G., Zhong, N., Peña, L. A., Smith, J. A., Martinez, S. R., Bacarian, T., Tammam, J., Ren, B., Farmer, P. M., Kalef-Ezra, J., Micca, P. L., Nawrocky, M. M., Niederer, J. A., Recksiek, F. P., Fuchs, A. & Rosen, E. M. (2002). *Neuro-oncology*, **4**, 26–38.

Fernandez-Palomo, C., Schültke, E., Smith, R., Bräuer-Krisch, E., Laissue, J., Schroll, C., Fazzari, J., Seymour, C. & Mothersill, C. (2013). *Int. J. Radiat. Biol.* **89**, 445–453.

Gehrmann, M., Specht, H. M., Bayer, C., Brandstetter, M., Chizzali, B., Duma, M., Breuninger, S., Hube, K., Lehnerer, S., van Phi, V., Sage, E., Schmid, T. E., Sedelmayr, M., Schilling, D., Sievert, W., Stangl, S. & Multhoff, G. (2014). *Radiat. Oncol.* **9**, 131.

Hadsell, M., Zhang, J., Laganis, P., Sprenger, F., Shan, J., Zhang, L., Burk, L., Yuan, H., Chang, S., Lu, J. & Zhou, O. (2013). *Appl. Phys. Lett.* **103**, 183505.

IAEA (2000). *Absorbed dose determination in external beam radiotherapy: an international code of practice for dosimetry based on standards of absorbed dose to water.* Technical Reports Series No. 398. International Atomic Energy Agency.

Kaplan, G. I., Rosenfeld, A. B., Allen, B. J., Booth, J. T., Carolan, M. G. & Holmes-Siedle, A. (2000). *Med. Phys.* **27**, 239–244.

Labiche, J.-C., Mathon, O., Pascarelli, S., Newton, M. A., Ferre, G. G., Curfs, C., Vaughan, G., Homs, A. & Carreiras, D. F. (2007). *Rev. Sci. Instrum.* **78**, 091301.

Pauline Fournier *et al.* • X-Tream QA in Synchrotron X-ray MRT

Laissue, J. A., Geiser, G., Spanne, P. O., Dilmanian, F. A., Gebbers, J.-O., Geiser, M., Wu, X.-Y., Makar, M. S., Micca, P. L., Nawrocky, M. M., Joel, D. D. & Slatkin, D. N. (1998). *Int. J. Cancer*, **78**, 654–660.

Lerch, M., Petasecca, M., Cullen, A., Hamad, A., Requardt, H., Bräuer-Krisch, E., Bravin, A., Perevertaylo, V. & Rosenfeld, A. B. (2011). *Radiat. Meas.* **46**, 1560–1565.

Low, D. A. & Dempsey, J. F. (2003). *Med. Phys.* **30**, 2455–2464.

Martínez-Rovira, I., Sempau, J. & Prezado, Y. (2012). *Med. Phys.* **39**, 119–131.

Nakaguchi, Y., Araki, F., Ono, T., Tomiyama, Y., Maruyama, M., Nagasue, N., Shimohigashi, Y. & Kai, Y. (2015). *Radiol. Phys. Technol.* **8**, 73–80.

Niroomand-Rad, A., Blackwell, C. R., Coursey, B. M., Gall, K. P., Galvin, J. M., McLaughlin, W. L., Meigooni, A. S., Nath, R., Rodgers, J. E. & Soares, C. G. (1998). *Med. Phys.* **25**, 2093–2115.

Petasecca, M., Cullen, A., Fuduli, I., Espinoza, A., Porumb, C., Stanton, C., Aldosari, A., Bräuer-Krisch, E., Requardt, H., Bravin, A., Perevertaylo, V., Rosenfeld, A. B. & Lerch, M. L. F. (2012). *J. Instrum.* **7**, P07022.

Povoli, M., Alagoz, E., Bravin, A., Cornelius, I., Bräuer-Krisch, E., Fournier, P., Hansen, T.-E., Kok, A., Lerch, M., Monakhov, E., Morse, J., Petasecca, M., Requardt, H., Rosenfeld, A. B., Röhrich, D., Sandaker, H., Salomé, M. & Stugu, B. (2015). *J. Instrum.* **10**, P11007.

Qi, Z.-Y., Deng, X.-W., Huang, S.-M., Shiu, A., Lerch, M., Metcalfe, P., Rosenfeld, A. & Kron, T. (2011). *Int. J. Radiat. Oncol. Biol. Phys.* **80**, 1581–1588.

Régnard, P., Bräuer-Krisch, E., Troprès, I., Keyriläinen, J., Bravin, A. & Le Duc, G. (2008). *Eur. J. Radiol.* **68**, S151–S155.

Requardt, H., Renier, M., Brochard, T., Bräuer-Krisch, E., Bravin, A. & Suortti, P. (2013). *J. Phys. Conf. Ser.* **425**, 022002.

Rosenfeld, A., Kaplan, G., Kron, T., Allen, B., Dilmanian, A., Orion, I., Ren, B., Lerch, M. & Holmes-Siedle, A. (1999). *IEEE Trans. Nucl. Sci.* **46**, 1774–1780.

Rosenfeld, A. B., Siegbah, E. A., Brauer-Krish, E., Holmes-Siedle, A., Lerch, M. L., Bravin, A., Cornelius, I. M., Takacs, G. J., Painuly, N., Nettelback, H. & Kron, T. (2005). *IEEE Trans. Nucl. Sci.* **52**, 2562–2569.

Schültke, E., Juurlink, B. H., Ataelmannan, K., Laissue, J., Blattmann, H., Bräuer-Krisch, E., Bravin, A., Minczewska, J., Crosbie, J., Taherian, H., Frangou, E., Wysokinsky, T., Chapman, L. D., Griebel, R. & Fourney, D. (2008). *Eur. J. Radiol.* **68**, S142–S146.

Serduc, R., Berruyer, G., Brochard, T., Renier, M. & Nemoz, C. (2010). *J. Synchrotron Rad.* **17**, 325–331.

Serduc, R., Bouchet, A., Bräuer-Krisch, E., Laissue, J. A., Spiga, J., Sarun, S., Bravin, A., Fonta, C., Renaud, L., Boutonnat, J., Siegbahn, E. A., Estève, F. & Le Duc, G. (2009). *Phys. Med. Biol.* **54**, 6711–6724.

Serduc, R., Christen, T., Laissue, J., Farion, R., Bouchet, A., van der Sanden, B., Segebarth, C., Bräuer-Krisch, E., Le Duc, G., Bravin, A., Rémy, C. & Barbier, E. L. (2008). *Phys. Med. Biol.* **53**, 3609–3622.

Siegbahn, E., Bräuer-Krisch, E., Bravin, A., Nettelbeck, H., Lerch, M. & Rosenfeld, A. B. (2009). *Med. Phys.* **36**, 1128–1137.

Sprung, C. N., Yang, Y., Forrester, H. B., Li, J., Zaitseva, M., Cann, L., Restall, T., Anderson, R. L., Crosbie, J. C. & Rogers, P. A. (2012). *Radiat. Res.* **178**, 249–259.

Zeman, W., Curtis, H. & Baker, C. (1961). *Radiat. Res.* **15**, 496–514.

Zhen, H., Nelms, B. E. & Tomé, W. A. (2011). *Med. Phys.* **38**, 5477–5489.